FULL PAPER

# B₁ inhomogeneity correction of RARE MRI with transceive surface radiofrequency probes

**Paula Ramos Delgado**[1,2] ⬤ | **Andre Kuehne**[3] | **João S. Periquito**[1,2] ⬤ | **Jason M. Millward**[1] | **Andreas Pohlmann**[1] | **Sonia Waiczies**[1] ⬤ | **Thoralf Niendorf**[1,2,3]

[1]Berlin Ultrahigh Field Facility (B.U.F.F), Max Delbrück Center for Molecular Medicine in the Helmholtz Association, Berlin, Germany

[2]Experimental and Clinical Research Center, a joint cooperation between the Charité Medical Faculty and the Max Delbrück Center for Molecular Medicine in the Helmholtz Association, Berlin, Germany

[3]MRI.TOOLS GmbH, Berlin, Germany

**Correspondence**
Paula Ramos Delgado, Berlin Ultrahigh Field Facility (B.U.F.F.), Max Delbrück Center for Molecular Medicine, Robert-Rössle-Str. 10, 13125 Berlin, Germany.
Email: Paula.Ramos@mdc-berlin.de

**Purpose:** The use of surface radiofrequency (RF) coils is common practice to boost sensitivity in (pre)clinical MRI. The number of transceive surface RF coils is rapidly growing due to the surge in cryogenically cooled RF technology and ultrahigh-field MRI. Consequently, there is an increasing need for effective correction of the excitation field ($B_1^+$) inhomogeneity inherent in these coils. Retrospective $B_1$ correction permits quantitative MRI, but this usually requires a pulse sequence-specific analytical signal intensity (SI) equation. Such an equation is not available for fast spin-echo (Rapid Acquisition with Relaxation Enhancement, RARE) MRI. Here we present, test, and validate retrospective $B_1$ correction methods for RARE.

**Methods:** We implemented the commonly used *sensitivity correction* and developed an empirical *model-based* method and a *hybrid combination* of both. Tests and validations were performed with a cryogenically cooled RF probe and a single-loop RF coil. Accuracy of SI quantification and $T_1$ contrast were evaluated after correction.

**Results:** The three described correction methods achieved dramatic improvements in $B_1$ homogeneity and significantly improved SI quantification and $T_1$ contrast, with mean SI errors reduced from >40% to >10% following correction in all cases. Upon correction, images of phantoms and mouse heads demonstrated homogeneity comparable to that of images acquired with a volume resonator. This was quantified by SI profile, SI ratio (error < 10%), and percentage of integral uniformity (PIU > 80% in vivo and ex vivo compared to PIU > 87% with the reference RF coil).

**Conclusion:** This work demonstrates the efficacy of three $B_1$ correction methods tailored for transceive surface RF probes and RARE MRI. The corrected images are suitable for quantification and show comparable results between the three methods, opening the way for $T_1$ measurements and X-nuclei quantification using surface

transceiver RF coils. This approach is applicable to other MR techniques for which no analytical SI exists.

# 1 | INTRODUCTION

The ability of MRI to provide high spatial resolution images within short acquisition times is governed by the sensitivity conundrum, which balances the constraints of signal-to-noise (SNR), image contrast, spatial resolution, and temporal resolution.[1-5] Numerous approaches have been developed to improve SNR per scan time from the development of novel software-driven approaches (eg, parallel imaging,[6,7] compressed sensing[8]), to hardware improvements, including higher magnetic field strengths $(B_0)$[9-11] and the optimization of radiofrequency (RF) technology. The use of surface RF coils is common practice to boost sensitivity[12] in (pre)clinical MRI, predominantly with a receive-only RF coil design in combination with a volume RF coil used for excitation.[13] The use of transceiver (transmit-receive, TxRx) surface RF coils is increasing, in particular in human MRI at ultrahigh fields[14-22] where large volume body RF coils are not used for signal excitation and are not provided with ultrahigh field-MR scanners.

In preclinical research, the use of transceiver RF configurations has been dominated by cryogenically cooled RF probes (CRP) that provide significant SNR gains.[23-25] CRPs are sometimes also available as decoupled Rx-only configurations in combination with a room-temperature (RT) volume resonator for RF excitation, but are not as common as the Tx/Rx configuration.[26] By reducing thermal noise in the receiver circuitry (RF probe and preamplifier), SNR can be enhanced by a factor of up to 3-4 compared to conventional RT RF coils.[23] The SNR gain of a CRP can be exploited to increase spatial resolution, to reduce scan time, or to lower detection limits, especially for X-nuclei MRI.

A constraint of TxRx surface RF coil technology is the strong intrinsic spatial gradient (inhomogeneity) in both excitation $(B_1^+)$ field and coil sensitivity $(B_1^-)$.[12,13] Although the latter can be easily corrected,[27-34] non-uniform $B_1^+$ fields induce significant spatial variations in the excitation flip angle (FA), with the effective FA decreasing with increasing distance from the RF coil surface. The resulting $B_1^+$ inhomogeneities are more pronounced at higher field strengths.[35,36] This adverse effect reduces image homogeneity and affects the $T_1$ image contrast, representing a major challenge for applications for which absolute signal intensities are needed, such as $T_1$ mapping[37,38] and quantification techniques in X-nuclei MRI.[39,40]

Although partial mitigation of $B_1^+$ inhomogeneity can be achieved with adiabatic pulses,[41,42] dielectric materials,[43-46] or $B_1^+$ shimming,[47-49] retrospective $B_1^+$ correction approaches are most commonly used to achieve signal uniformity.[50-56] First, the actual FA is measured using magnitude- or phase-based $B_1^+$ mapping techniques, such as the double angle method,[57,58] the phase sensitive technique,[59] the actual FA method,[60] or any of their improvements.[61-63] Then, an analytical description of the signal intensity (SI) dependency on the FA for the RF pulse sequence (SI equation)[50-54] or numerical simulations[55,56] are used to perform the SI correction.

Retrospective $B_1^+$ correction has been successfully applied to gradient echo imaging techniques such as fast low angle shot[50,51] or steady-state free precession,[54] which are inherently less sensitive to RF inhomogeneity[64] and for which SI equations are given.[65] Retrospective $B_1^+$ correction was also reported for spin-echo imaging methods.[52,53] For fast spin-echo techniques such as Rapid Acquisition with Relaxation Enhancement (RARE)[66] there is no exact analytical SI equation.[67,68] This extends to pulse sequences employing simultaneous multislice parallel imaging,[69] non-Cartesian trajectories,[70-72] variable FA 3D turbo spin-echo,[73] water-fat separation using Dixon approaches,[74] and hybrid imaging techniques like half-Fourier single shot turbo spin-echo/gradient and spin-echo/turboGRASE (HASTE/GRASE/TGSE).[75] Other complex techniques with no SI equation include those derived from ultrashort echo time[76] or echo-planar imaging (EPI).[77] As a consequence, retrospective $B_1^+$ correction for these MRI techniques demands novel solutions.

To address this need, we developed, implemented, and applied three $B_1$ correction approaches for RARE MRI with transceive surface RF probes with the goal to reduce errors to less than 10% for SI quantification and for $T_1$ contrast. All three methods were applied and validated in test phantoms and mouse brains, in vivo and ex vivo. For performance evaluation, the corrected images were benchmarked against reference images obtained with a uniform TxRx volume resonator. The starting point was the commonly used *sensitivity correction*[27] that uses a uniform phantom image to correct for $B_1^-$ inhomogeneities. This method does not take spatial FA variations and $T_1$ relaxation times into account. Given this limitation and the unavailability of an analytical SI equation for fast spin-echo imaging, we modelled the SI of RARE as a function of FA and $T_1$ based on empirical measurements obtained through MR experiments. This *model-based correction* uses the SI model to correct $B_1^+$, followed by a $B_1^-$ correction. We also implemented a *hybrid correction* using a combination of the *model-based* and *sensitivity correction* approaches. These methods are valuable not only for conventional $^1$H-MRI when

accurate FAs are needed (eg, for well-defined $T_1$ contrasts), but also in X-nuclei MRI, for which absolute SI is essential for signal quantification.

## 2 | METHODS

The MR hardware, sample preparation, and measurements are summarized in Table 1.

### 2.1 | MR hardware

All experiments were performed on a 9.4 T small animal MR scanner (BioSpec 94/20, Bruker BioSpin, Ettlingen, Germany) operating at 400 MHz ($^1$H).

For creating reference images, we chose RF coils with approximately uniform excitation and reception fields:

- Small reference RF coil: in-house built volume resonator tailored for mouse head imaging[78] (inner diameter [ID] = 18.4 mm).
- Large reference RF coil: rat body linear volume resonator (Bruker BioSpin) with an ID = 72 mm.

The correction methods were applied, evaluated, and validated for 2 transceive surface RF coils:

- Cryocooled surface RF coil (CRP): 2-element transceive RF probe (CryoProbe®, Bruker BioSpin) operating in quadrature mode with an ID = 20 mm and a saddle-shaped ceramic surface.
- RT surface RF coil: planar transceive single loop (ID = 20 mm) surface RF coil (Bruker BioSpin).

### 2.2 | Sample and animal preparation

To characterize the excitation and receive fields of the transceive surface RF coils ($B_1$ mapping), we used samples that ensured full field of view coverage and had low $T_1$ values ($T_1 \approx 300$ ms) to reduce the needed TR (TR > 5·$T_1$) in our measurements:

- Cylindrical uniform phantom with low $T_1$: 15-mL tube (ID = 14.6 mm, length = 120 mm; Thermo Fisher Scientific, Waltham, Massachusetts) filled with a mixture of water and copper sulfate (Carl Roth GmbH & Co. KG, Karlsruhe, Germany).
- Rectangular uniform phantom with low $T_1$: 50-mL cell culture flask (($79.7 \times 42.6 \times 25$) mm$^3$; Fisher Scientific) filled with a doped solution of water.

Samples with different $T_1$ (NMR tubes, Thermo Fisher Scientific) filled with aqueous solutions of gadolinium (Magnevist® 0.5 mmol/ml; Bayer Vital, Leverkusen, Germany) at different concentrations (0-0.5 mM) yielding $T_1$ between 190 and 2871 ms were used to produce the RARE SI models.

The test phantoms used for correction and evaluation of the $B_1$ correction methods were:

- Cylindrical uniform phantom: containing water doped with gadolinium embedded in a 15-mL tube ($T_1 \approx 800$ ms).
- Ex vivo mouse: the central nervous system of a SJL/J female mouse, perfused with a phosphate-buffered saline (Biochrom GmbH, Berlin, Germany), fixed in paraformaldehyde (PFA; Santa Cruz Biotechnology, Inc., Dallas,Texas), and placed into a 15-mL tube filled with 4% PFA.
- In vivo mouse: a healthy SJL/J mouse anesthetized with 2.7% isoflurane and stabilized with 1.6% during scanning. Heart rate, respiration rate, and temperature were monitored and kept constant during the examinations.
- Rectangular uniform phantoms: four 50-mL cell culture flasks filled with solutions of two different $^1$H-atom concentrations: 100% water, 50% water and 50% deuterium oxide (Sigma-Aldrich, Saint Louis, Missouri). Gadolinium was added to the mixtures to achieve two different $T_1$ values (490 and 1525 ms).

All animal experiments were approved by the Animal Welfare Department of the LAGeSo State Office of Health and Social Affairs in Berlin and in accordance with international guidelines on reduction of discomfort (86/609/EEC).

### 2.3 | MR measurements

To characterize the $B_1$ fields of both transceive surface RF coils we used:

- FA mapping: fast low angle shot (FLASH) measurements with nominal excitation FAs of 60°/120° (RT) and 60°/120°/240° (CRP) with echo time/pulse repetition time (TE/TR) = 2.49/2000 ms, matrix = 128 × 128, 3 slices with a gap of 0.5 mm and a thickness of 2 mm each, TA = 1h30. We used a field of view = (25 × 25) mm$^2$ for the CRP and field of view = (35 × 35) mm$^2$ for RT.
- $B_1^-$ mapping: FLASH measurement with a nominal FA of 5° (same parameters as above).

$B_1$ field characterization can be performed prior to or after the image acquisition and does not entail extra acquisition time on the day of image acquisition, for example, in vivo scans.

**TABLE 1** Detailed overview of measurements

| Purpose | MR protocol | RF coil type | RF coil | Sample(s) | Acq. time |
|---|---|---|---|---|---|
| Test images | $T_1$w-RARE (with flipback) | Surface TxRx | CRP | Cylindrical uniform phantom | 60 min |
| | | | | Ex vivo mouse | 60 min |
| | | | | In vivo mouse | 30 min |
| Validation images | $T_1$w-RARE (with and w/o flipback) | Surface TxRx | RT | Rectangular uniform phantoms | 30 min |
| Sensitivity correction | | | | | |
| Uniform phantom images | $T_1$w-RARE (with and w/o flipback) | Surface TxRx | CRP | Cylindrical uniform phantom with low $T_1$ | 60 min |
| | $T_1$w-RARE (with and w/o flipback) | Surface TxRx | RT | Rectangular uniform phantom with low $T_1$ | 30 min |
| Model-based correction | | | | | |
| Mapping of FA and $B_1^-$ | FLASH | Surface TxRx | CRP | Cylindrical uniform phantom with low $T_1$ | 90 min per FA |
| | FLASH | Surface TxRx | RT | Rectangular uniform phantom with low $T_1$ | 30 min per FA |
| RARE SI modelling | $T_1$w-RARE (with and w/o flipback) | Volume TxRx | Small reference RF coil | Samples with different $T_1$ | 5 m 40 s per FA |
| $T_1$ mapping for modelling | RARE with variable TR | Volume TxRx | Small reference RF coil | Samples with different $T_1$ | 90 min |
| $T_1$ mapping for test images | RARE with variable TR | Volume TxRx | Small reference RF coil | Cylindrical uniform phantom | 100 min |
| | | | | Ex vivo mouse | 30 min |
| | | | | In vivo mouse | 55 min |
| $T_1$ mapping for validation images | RARE with variable TR | Volume TxRx | Large reference RF coil | Rectangular uniform phantoms | 30 min |
| Hybrid correction | | | | | |
| Mapping of FA and $B_1^-$ | FLASH | Surface TxRx | CRP | Cylindrical uniform phantom with low $T_1$ | 90 min per FA |
| | FLASH | Surface TxRx | RT | Rectangular uniform phantom with low $T_1$ | 30 min per FA |
| RARE SI modelling | $T_1$w-RARE (with and w/o flipback) | Volume TxRx | Small reference RF coil | Samples with different $T_1$ | 5 m 40 s per FA |
| $T_1$ mapping for modeling | RARE with variable TR | Volume TxRx | Small reference RF coil | Samples with different $T_1$ | 90 min |
| $T_1$ mapping for test images | RARE with variable TR | Volume TxRx | Small reference RF coil | Cylindrical uniform phantom | 100 min |
| | | | | Ex vivo mouse | 30 min |
| | | | | In vivo mouse | 55 min |
| $T_1$ mapping for validation images | RARE with variable TR | Volume TxRx | Large reference RF coil | Rectangular uniform phantoms | 30 min |
| $T_1$ mapping uniform phantom | RARE with variable TR | Volume TxRx | Small reference RF coil | Cylindrical uniform phantom with low $T_1$ | 100 min |
| $T_1$ mapping uniform phantom | RARE with variable TR | Volume TxRx | Large reference RF coil | Rectangular uniform phantom with low $T_1$ | 30 min |

CRP, cryogenically cooled radiofrequency probes; FA, flip angle; FLASH, fast low angle shot; RARE, Rapid Acquisition with Relaxation Enhancement; RT, room temperature; TxRx, transmit-receive.

To compute the models, we performed RARE measurements both with and without flipback and studied the effect of the extra pulse (which restores longitudinal magnetization, improving SNR) on the SI:

- $T_1$-weighted ($T_1$w-) RARE scans (TE/TR = 2.49/1000 ms, echo train length (ETL) = 8, receiver bandwidth = 50 kHz, centric phase encoding, field of view = (25 × 25) mm$^2$, matrix = 128 × 128, 3 slices of 2 mm thickness,

TA = 5m40s). Thirty-five reference RF powers were used to vary the excitation FA in 5° increments, between 5° and 160° (flipback) and between 5° and 110° (without flipback).

- $T_1$ maps of all phantoms (RARE with variable TR (120-15 000 ms); ETL = 2, linear phase encoding, other parameters same as RARE scan).

$T_1$w-RARE images were acquired using the same parameters as above with flipback (CRP) and with/without flipback (RT) for validation purposes. Corresponding $T_1$ maps for all samples were measured using RARE with TR ranging from 150 to 14500 ms.

All reference RF power adjustments were performed on a 2-mm slice located parallel and close to the RF coil surface.

RARE modeling can be equally performed prior to or after the image acquisition and does not entail extra acquisition time on the day of image acquisition, for example, in vivo scans.

## 2.4 | Approach 1: Sensitivity correction

All post-processing was performed using customized software developed in MATLAB (MathWorks Inc., Natick, Massachusetts).

This straight-forward method only requires a uniform phantom image to correct for the $B_1^-$ inhomogeneities.[27,28] The following steps were performed (Figure 1A):

- MRI study. Images (sample and uniform phantom) were acquired.
- Correction factor computation. We normalized and calculated the inverse of the uniform phantom image.
- Sensitivity correction. We multiplied the uncorrected image by the estimated correction factor to correct for the $B_1^-$ inhomogeneities.

This method requires neither the characterization of the transceive RF coil used, nor the calculation of a RARE SI model and it is, therefore, directly applicable after image acquisition with little post-processing.

## 2.5 | Approach 2: Model-based correction

Figure 2 shows the workflow of the model-based correction, consisting of the following steps, starting with the quantification of the $B_1$ inhomogeneities:
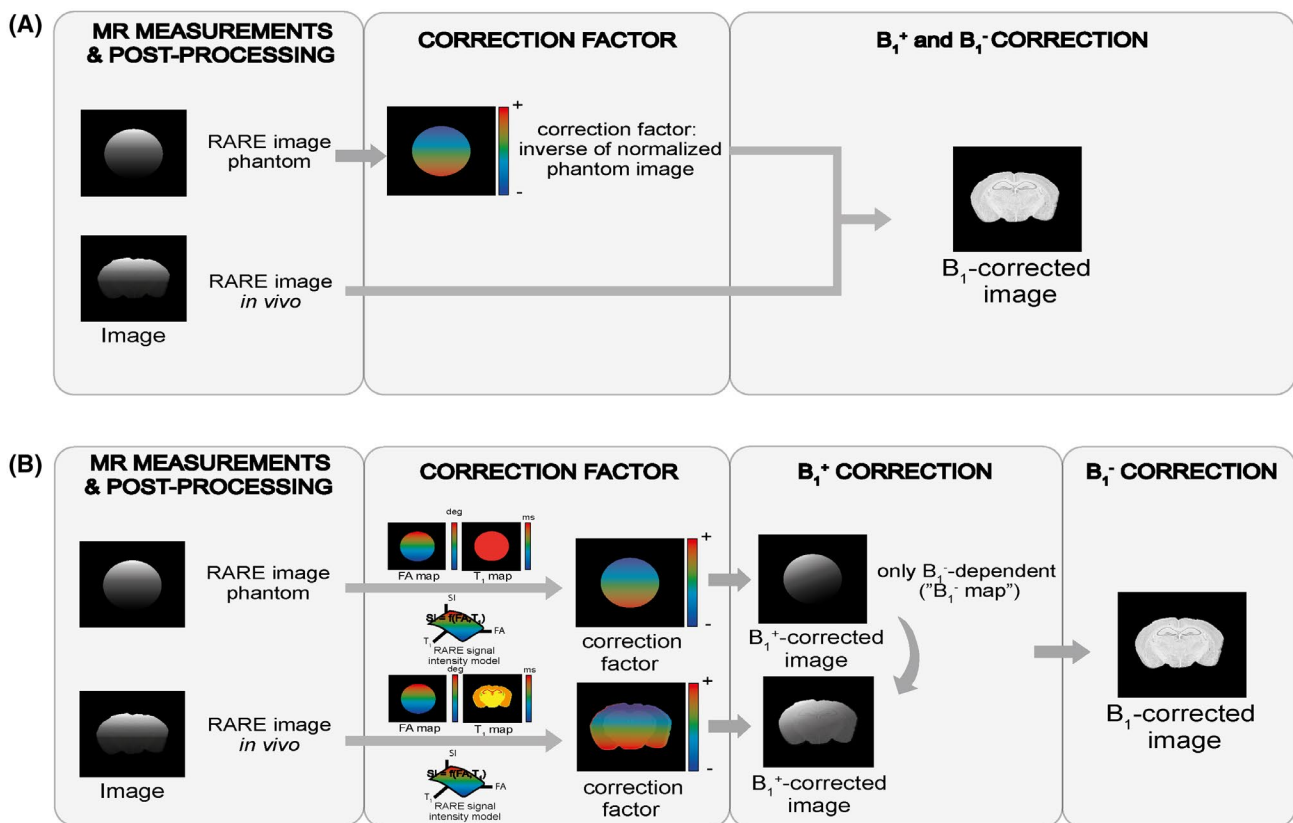


**FIGURE 1** Workflows of (A) sensitivity correction and (B) hybrid $B_1$ correction. The sensitivity correction merely requires dividing the sample image by that of a normalized uniform phantom. The hybrid method combined the model-based approach to perform a $B_1^+$ correction on the sample image and a uniform phantom image. The latter is then used to perform a $B_1^-$ correction using the sensitivity correction method
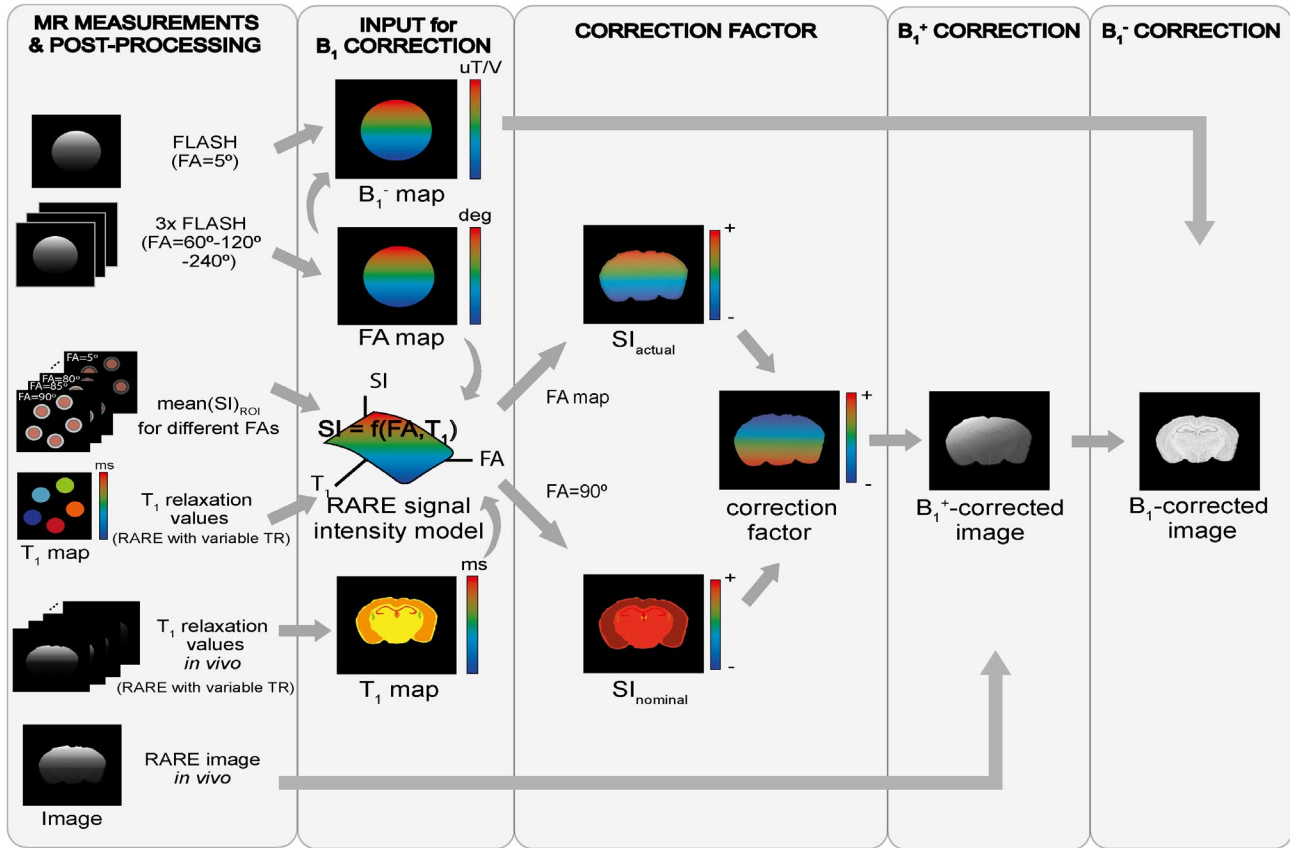
**FIGURE 2** Workflow of model-based $B_1$ correction. The necessary images and maps to be acquired are described in MR Measurements & Post-processing column. Then the flip angle (FA) and sensitivity ($B_1^-$) maps were calculated using the double angle method and the low FA approximation, respectively. The Rapid Acquisition with Relaxation Enhancement (RARE) signal intensity model was derived from a 2D fit of the signal intensities measured for different FAs and $T_1$ relaxation times using a volume resonator. The $B_1^+$ correction factor was computed pixel-wise for the actual FA and $T_1$ using the RARE signal intensity model. Applying this correction factor and the $B_1^-$ map derived correction factor yielded the final $B_1$ corrected image

- RF coil characterization. *FA maps* were calculated using the double angle method.[57,58] To increase the SNR distal to the CRP we added a measurement at a higher FA and merged the 60°/120° and 120°/240° maps using an SNR cutoff. All maps were denoised using a polynomial fitting tool (*polyfitn*,[79] 10th-order polynomials).

The *transmit field ($B_1^+$) maps* were computed using:

$$FA = \gamma \cdot B_1^+ \cdot \tau$$

with $\gamma$ being the gyromagnetic ratio ($\gamma = 267.522 \cdot 10^6$ rad s$^{-1}$ T$^{-1}$ for $^1$H) and $\tau$ the pulse length of a rectangular RF pulse. Because calculated RF pulses were used, each one has a complex shape tailored to the sequence parameters. We therefore approximated the RF pulse length $\tau$ using the product of the RF pulse duration, the area under the RF pulse ($S_{int}$), and the related voltage (V):

$$B_1^+ = \frac{FA \cdot \pi/180}{\gamma \cdot t_p \cdot S_{int} \cdot V}$$

The *RF coil sensitivity maps ($B_1^-$)* were calculated using the low FA approximation[80,81]:

$$SI_{lowFA} \propto \left| B_1^+ \right| \cdot \left| B_1^- \right|$$

where $SI_{lowFA}$ was the 5° fast low angle shot measurement. The low FA image and $B_1^+$ map were normalized by their respective maximum values and $B_1^-$ calculated as:

$$B_1^- / \max\left(B_1^-\right) \propto \frac{B_1^+ / \max\left(B_1^+\right)}{SI_{lowFA} / \max\left(SI_{lowFA}\right)}$$

Ultimately, the $B_1^-$ map was denoised using a 10th-order polynomial fit.

- Modeling of the RARE SI equation. The relationship between SI, FA, and $T_1$ was estimated using experimental data and a fitting tool:

Data analysis: Images were denoised using a spatially adaptive non local means filter,[82] and $T_1$ maps computed

by fitting $S = S_0(1-\exp(-TR/T_1))$ to the SIs using in-house developed software in MATLAB. We assumed $SI(FA = 0°) = 0$ for all $T_1$. For each $T_1$ sample, a circular region of interest (ROI) was drawn to extract average SI and $T_1$ values from the images and maps respectively.

RARE modeling: To model the $SI = f(FA,T_1)$ relationship a $7^{th}$-order 2D polynomial was fitted to the experimental data using MATLAB's *polyfitn*[79] function. This was the lowest polynomial order that gave an $R^2 > 0.99$ and a faithful representation of the measured data.

- MRI study. Images and corresponding $T_1$ maps of the test samples were acquired.
- Retrospective correction. All images and maps ($B_1^+/B_1^-/T_1$) were spatially aligned, either by careful slice planning or by image registration.

The $B_1^+$-correction factor ($f_{corr}$) was calculated as the modeled RARE SI for a perfect 90° excitation ($SI_{nominal}$) divided by the modeled RARE SI for the actual excitation FA ($SI_{actual}$) obtained from the FA map:

$$f_{corr} = \frac{SI_{nominal}}{SI_{actual}}$$

Applying this correction factor yielded a $B_1^+$-corrected image:

$$image_{B1+corr} = image \cdot f_{corr}$$

In the few cases where the algorithm produced negative values (low-SNR regions), the correction factor was set to zero.

Dividing this $B_1^+$-corrected image by the $B_1^-$ map produced the final $B_1$-corrected image:

$$image_{corr} = image_{B1+corr}/B_1^-$$

## 2.6 | Approach 3: Hybrid correction

This method combines the sensitivity and model-based correction (workflow in Figure 1B), and involves:

- RF coil characterization (as in *Model-based Correction*).
- Modeling of the RARE SI equation (as in *Model-based Correction*).
- MRI study. Images and $T_1$ maps of the samples and of a uniform phantom were measured.
- Model-based $B_1^+$ correction (as in *Model-based Correction*) was performed on the sample and uniform phantom image.

- $B_1^-$ correction (as in *Sensitivity Correction*). The inverse of the $B_1^+$-corrected uniform phantom image was applied as the $B_1^-$ correction factor to the $B_1^+$-corrected sample image.

Both the model-based and the hybrid correction methods need a prior/posterior characterization of the transceive RF coil used and the calculation of a RARE SI model. The post-processing needed is rather simple in both cases.

## 2.7 | Correction method evaluation and validation

The presented $B_1$ correction techniques were validated using the following methods:

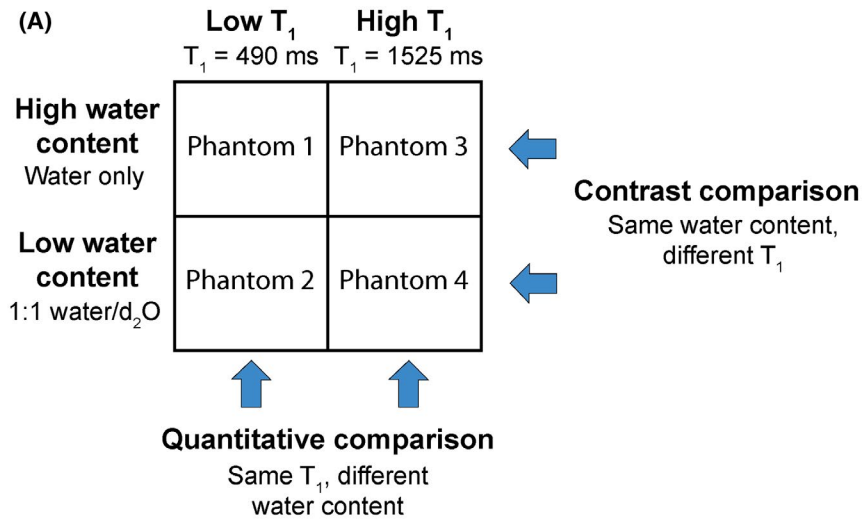### 2.7.1 | Central profile plots

The SI profile along a central line perpendicular to the RF coil surface was plotted against distance to the RF coil surface. Seven pixels across the width of the line were averaged, and the SIs were normalized to [0,1] to allow a better comparison. A quantitative comparison was performed by calculating the root-mean-square-error (RMSE) between each profile and the reference. Each profile was scaled to minimize the RMSE against the reference, in order to compensate for the arbitrary scaling and to provide a fair comparison.

### 2.7.2 | Image homogeneity assessment

To quantitatively assess the uniformity of the corrected images, the *percentage of integral uniformity* (PIU)[83] was computed for several ROIs of different sizes. A PIU of 100% represents perfect image homogeneity. In the uniform phantom, we defined 5 internally tangential circular regions of interest (ROIs) with increasing diameter on the central vertical line. For the brain images (ex vivo, in vivo), we manually outlined the cortex and basal ganglia/thalamus (left and right), achieving 3 ROIs.

### 2.7.3 | $T_1$-contrast and quantification performance

We used the experimental setup (Figure 3A) to compare substances with different water content (100% or 50%, respectively) and different $T_1$ relaxation times (490 or 1525 ms, respectively). All acquired images with and without flipback were corrected using the three $B_1$ correction methods. Five ROIs were drawn at

**(A)**

| | Low $T_1$<br>$T_1$ = 490 ms | High $T_1$<br>$T_1$ = 1525 ms |
|---|---|---|
| **High water content**<br>Water only | Phantom 1 | Phantom 3 |
| **Low water content**<br>1:1 water/d$_2$O | Phantom 2 | Phantom 4 |

**Contrast comparison**
Same water content, different $T_1$

**Quantitative comparison**
Same $T_1$, different water content

**(B)**

Quantitative comparison for low $T_1$ (example):

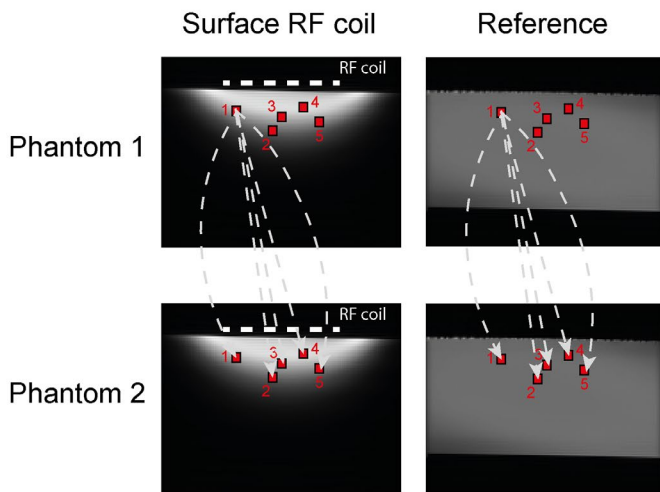Surface RF coil    Reference

Phantom 1

Phantom 2

**FIGURE 3** Illustrations of validation methods. (A) To evaluate the performance of the correction methods (sensitivity, model based, and hybrid), 4 phantoms with different water content and $T_1$ relaxation times were prepared. The quantitative assessment compared flasks with different water content for both low and high $T_1$ values. Similarly, contrast was evaluated by comparing phantoms with different $T_1$ values at low and high water content. (B) shows the region of interest (ROI) placement and depicts for one selected ROI the ratios that were calculated. In this manner we calculated the ratios for all possible ROI combinations in the corrected, original and reference images. The mean relative errors of these ratios with regard to those obtained in the reference served as quantitative measure for the validation

pseudo-randomized positions (Figure 3B) on all sets of images (three corrections, original and reference) for all flasks. For each of the flask image pairs described in Figure 3A, mean SI ratios were calculated using all possible ROI combinations for all sets. Relative ratio errors were computed:

$$\text{Ratio error} = \frac{\text{abs}\left(\overline{\text{SI}}\text{reference} - \overline{\text{SI}}\text{corrected}\right)}{\overline{\text{SI}}\text{reference}} * 100(\%)$$

With $\overline{\text{SI}}$reference being the mean SI ratio computed using all ROI combinations on the reference image pairs, and $\overline{\text{SI}}$corrected being that achieved using the corrected image pairs. Finally, the mean error and mean SD were calculated. An example of the workflow is shown in Figure 3B.

Statistical analysis. A nonparametric 1-way analysis of variance Friedman repeated measures test was performed (mean errors on the original data did not have a Gaussian distribution) followed by Dunn's test where all corrections were compared to the original data ($P$ values < .05 were considered

significant). All statistical assessments were performed using GraphPad Prism 5 (GraphPad Software, La Jolla, California).

## 3 | RESULTS

### 3.1 | RF coil characterization

The maps of the receive field ($B_1^-$) (Figure 4A) and transmit field ($B_1^+$, here as FA) relative to a 90° excitation FA (Figure 4B) demonstrate the spatially varying sensitivity and FA for the CRP. A closer look at the vertical midline profile reveals a strong deviation from the target of FA = 90° (nominal FA) with increasing distance from the surface of the CRP (Figure 4C). These field maps show the typical inhomogeneity inherent to transceive surface RF coils, which was very similar in the $B_1^+$ and $B_1^-$ maps and FA profiles for the single loop RF coil (Figure 4D-F). The minor deviation of the FA profiles at 20-30 mm from the coil surface (in gray) reflects a mathematical artifact of the polynomial fit at low-SNR regions
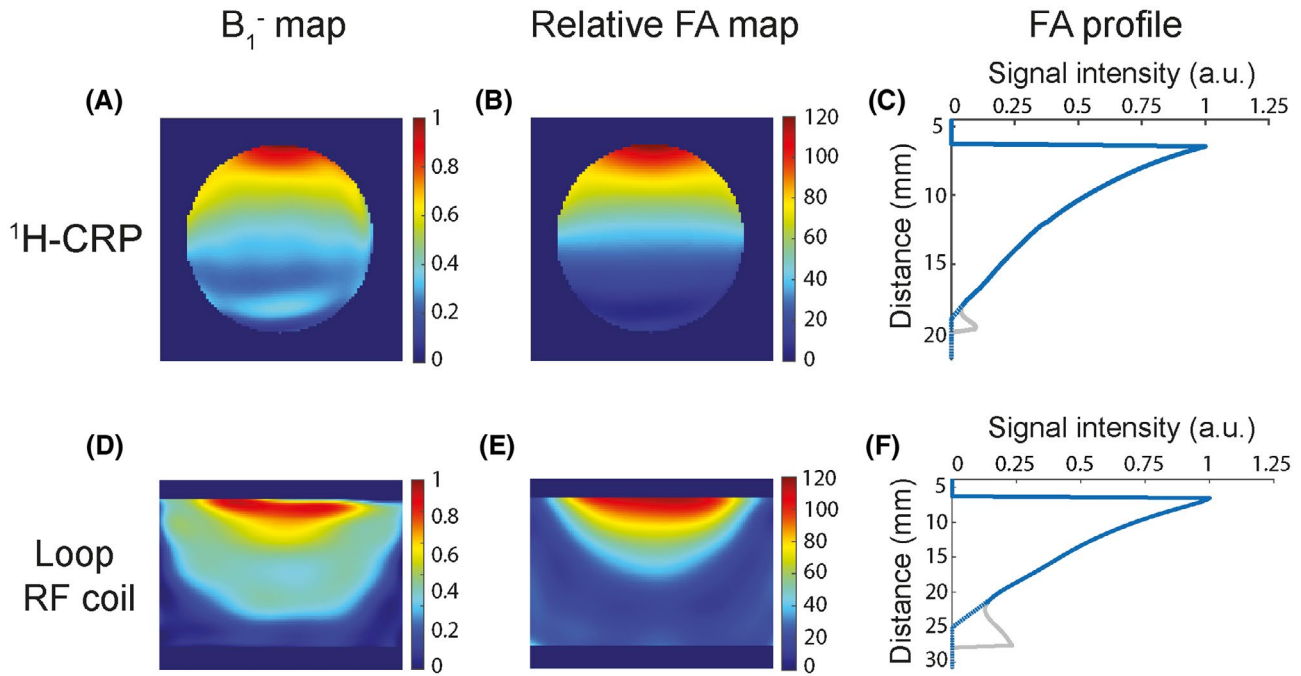
**FIGURE 4** Sensitivity maps and transmission fields of the two transceive (TxRx) surface radiofrequency (RF) coils used for testing and validation. (A,D) Axial view of the computed sensitivity ($B_1^-$) maps for a uniform phantom placed close to the RF coil surface. (B,E) Corresponding flip angle (FA) maps relative to a 90° excitation. (C,F) Normalized central profile plots of the FA along the vertical axis, which reveal a strong decay with increasing distance to the RF coil surfaces. The gray lines depict the true calculated data misestimated by the polynomial fit at low signal-to-noise ratio regions far away from the RF coil surface; the assumed true value is shown by the blue dotted lines

far from the RF coil surface. The assumed correct value is depicted by the dashed blue line.

## 3.2 | Modeling of the RARE SI equation

The RARE SI dependency on FA and $T_1$ (SI = f(FA,$T_1$)) was modeled by fitting a polynomial to the experimental data acquired with these parameters, either incorporating a flipback pulse to restore longitudinal magnetization and hence improve SNR (Figure 5A-C), or excluding flipback to allow natural relaxation (Figure 5D-F). The fitted 3D-surfaces are shown in Figure 5A,D. Two-dimensional projections of the RARE models show the relationships between SI and $T_1$ for several FA values (Figure 5B,E) and between SI and FA for several $T_1$ values (Figure 5C,F). As expected, the fitted SI data predicts lower SI with increasing $T_1$ and maximal SI for FAs around 90°. The surface fits modeled the experimental data well ($R^2 = 0.997$ in both cases).

## 3.3 | Correction method evaluation and validation

We acquired $T_1$ maps (needed for $B_1^+$ correction) and reference images of a uniform phantom, an ex vivo mouse phantom, and an in vivo mouse brain using a volume resonator

(Figure 6A-B). The original uncorrected CRP images show the strong spatial SI gradient typical of transceive surface RF coils (Figure 6C). The results obtained with the three $B_1$ correction methods are shown in Figure 6D-F. The strong spatial SI gradient present in the CRP images was removed by all $B_1$ correction methods, yielding a uniform SI throughout the entire field of view for all investigated samples, including the in vivo mouse head. With the *sensitivity* and *model-based corrections* we observed an overshoot in SI in some regions, particularly distal to the CRP. This was due to a combination of increasing inaccuracies in the FA and SI data at low SNR. This overshoot in SI was resolved by combining both methods in the hybrid correction approach.

### 3.3.1 | Central profile plots (CRP)

To quantitatively assess the correction of the image inhomogeneity, we plotted normalized vertical SI profiles (Figure 7A-C). For all three approaches, the corrected SI profiles showed close correspondence with the reference RF coil (plotted as a surface in green). From these profiles one can determine how far away from the RF coil it is still viable to perform $B_1$ correction. This depends on the specific scanning parameters and the dimensions of the RF coil; here this distance was approximately 17 mm (for a nominal FA of 90°, an actual FA of up to 8° could be
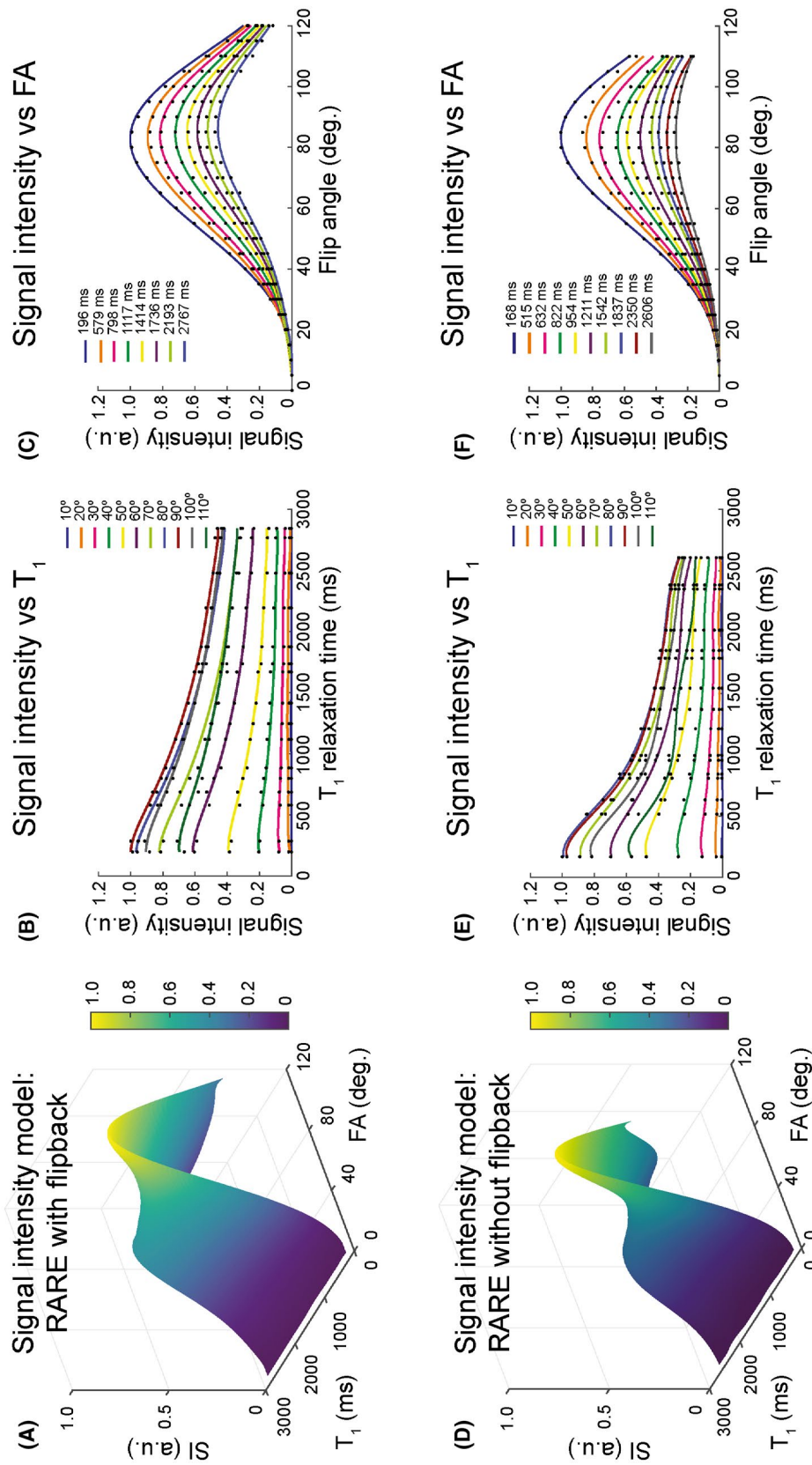
**FIGURE 5** Signal intensity (SI) models for Rapid Acquisition with Relaxation Enhancement (RARE) with and without flipback. (A,D) 3D-plots of the modelled RARE signal intensity (SI) as a function of the $T_1$ relaxation time and flip angle (FA) with and without flipback, respectively ($R^2 = 0.997$ for both). (B,E) show the SI vs FA projection in both models, whereas (C,F) depict the SI vs $T_1$ projection. Selected FA and $T_1$ values are plotted to demonstrate the fidelity of the experimental data and the model. Each colored line depicts a different $T_1$ and FA, respectively. The dots represent the measured data points
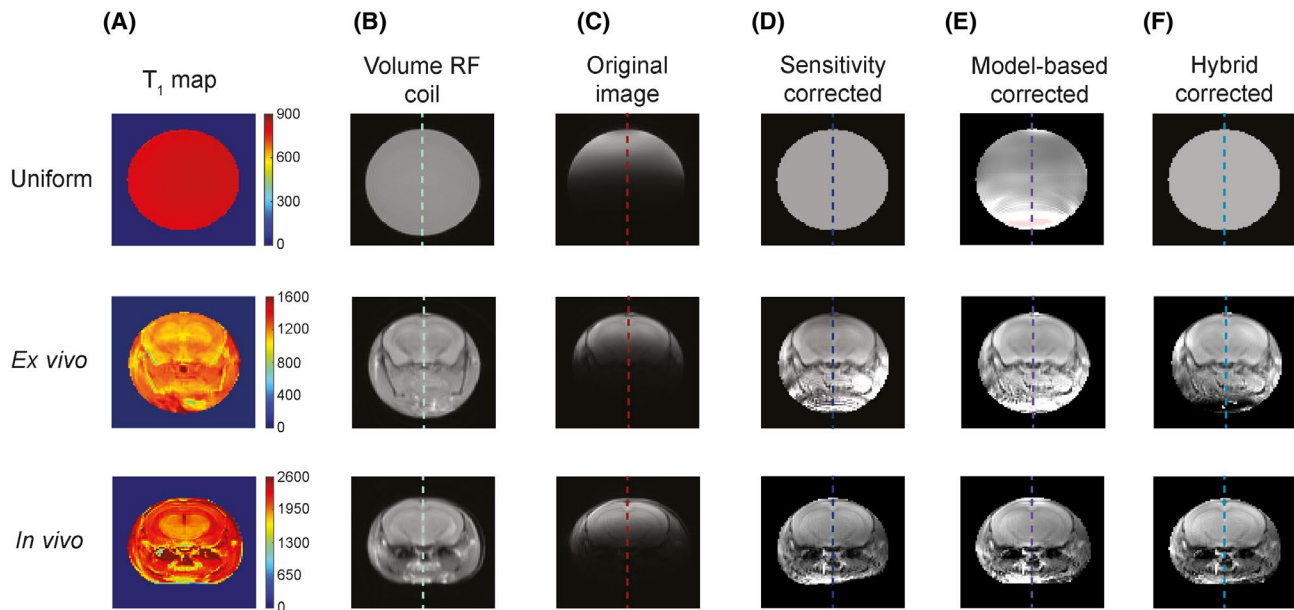
**FIGURE 6** $B_1$ correction for cryogenically cooled radiofrequency probes (CRP) images of a uniform phantom, an ex vivo phantom and a living mouse. From left to right, the columns show (A) the acquired $T_1$ map (reference coil), (B) the reference image, (C) the original CRP image, (D-F) the corrected images. A comparison of the original images with the reference images demonstrates the need of $B_1$ correction. Quantification is severely hampered by the adverse signal intensity gradient. The corrected images show a remarkably improved homogeneity. All three correction methods performed well, with only slight differences between the results. Masks containing minor errors in the correction are overlaid and shown in light red

corrected). For our experimental setup, the region beyond 17 mm showed increasing inaccuracies in the field maps and SI measurements, leading to unacceptable errors in all corrected images.

Quantitative examination revealed that all correction methods considerably reduced the RMSE computed on the profiles to a maximum of 0.18 (uniform), 0.12 (ex vivo) and 0.26 (in vivo), with respect to the reference. For the uniform phantom, the *sensitivity* and *hybrid approaches* performed equally well (0.11). For the ex vivo phantom the *sensitivity* and *model-based correction* performed similarly (0.11). In vivo, the *sensitivity correction* achieved the best result (0.21). In comparison, the uncorrected profiles revealed an average RMSE of $0.53 \pm 0.07$ for all test phantoms.

### 3.3.2 | Image homogeneity assessment (CRP)

For the uniform phantom, we found the calculated PIU (Figure 7D-F) to be 95.7% within the largest ROI using the volume resonator, indicating no significant inhomogeneities across the image, as expected. Conversely, a PIU of 0.9% was obtained within the same ROI on the uncorrected image. The PIU degradation scaled with increasing ROI diameter. After correction, the *model-based approach* showed a PIU of 65% on the fourth ROI (up to a distance of 16.2 mm from the RF coil surface). Beyond that distance, the observed overshoots

confounded the PIU, which decreased to 0% in the largest ROI.

For the mouse brain images the PIUs showed the expected high homogeneity for the reference RF coil: ex vivo $87.0 \pm 4.4\%$ and in vivo $87.7 \pm 9.1\%$. The original surface RF coil images displayed substantial inhomogeneities: averages of $35.4 \pm 9.2\%$ ex vivo and $33.2 \pm 11.8\%$ in vivo. A significant improvement in image homogeneity was achieved with all three correction methods, both in vivo and ex vivo. The *model-based method* performed best on average ($85.0 \pm 3.8\%$ ex vivo and $80.5 \pm 11.3\%$ in vivo), closely followed by the *hybrid* ($81.6 \pm 6.9\%$ ex vivo and $79.7 \pm 11.2\%$ in vivo) and *sensitivity* ($80.8 \pm 5.7\%$ ex vivo and $76.5 \pm 10.3\%$ in vivo) *corrections*.

### 3.3.3 | $T_1$-contrast and quantification performance (RT)

We studied the errors in SI ratios between several fixed locations for all four phantoms, comparing original (uncorrected) RARE images and their three corrections, relative to the ground truth (reference images). These validation assessments were performed for RARE without flipback (Figure 8) and with flipback (Figure 9). The box plots (whiskers at 5-95 percentile) depict the mean errors for quantification at low and high $T_1$ relaxation times, and for $T_1$ contrast measurements with low and high proton
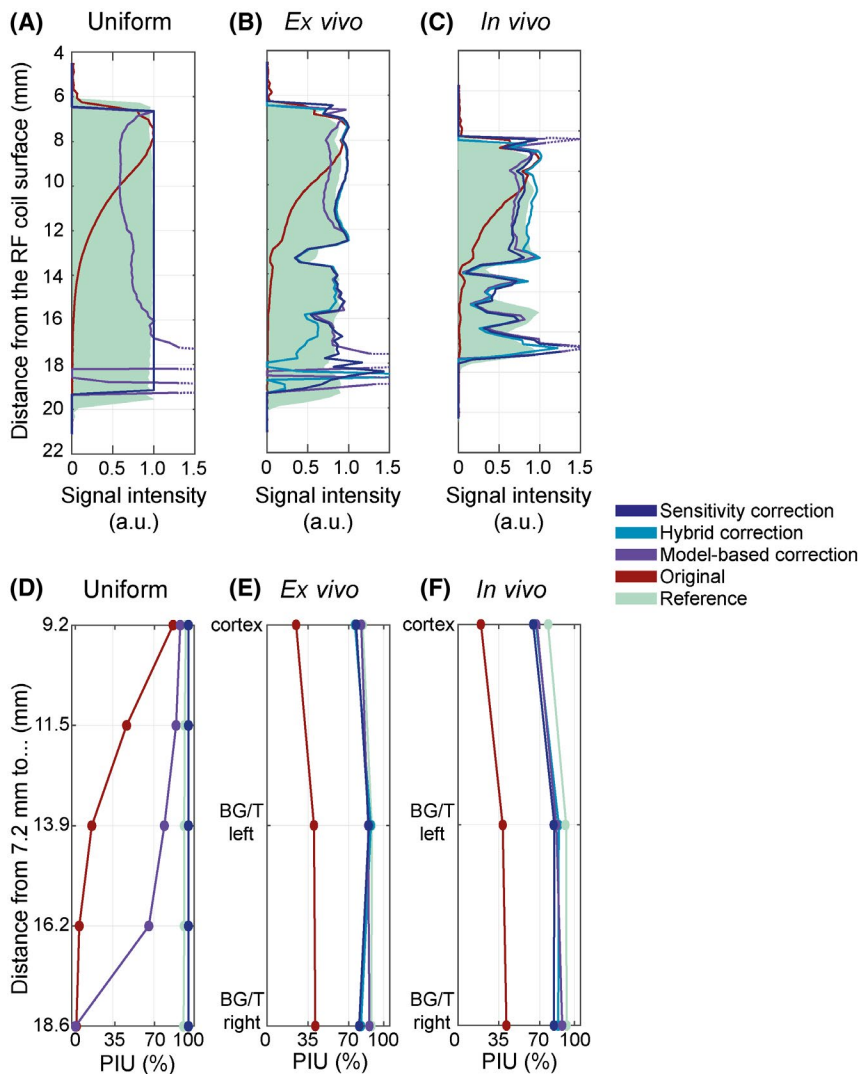
**FIGURE 7** Normalized signal intensity profiles perpendicular to the radiofrequency (RF) coil surface and percentage of integral uniformities (PIU) for the exemplary images shown in Figure 5: (A-D) uniform phantom, (B-E) ex vivo, and (C-F) in vivo, using 5 internally tangent circular regions of interest (ROIs) with increasing diameter (uniform) or anatomical regions (ex vivo, in vivo: cortex and basal ganglia/thalamus, BG/T). The corrected profiles demonstrate a striking increase in image homogeneity and show the same trends as those of the reference coil. In all three phantoms the calculated root-mean-square-errors (RMSEs) of the corrected profiles reveal a high resemblance to the reference. The PIU plots indicate a significant improvement in image homogeneity after correction

density. Errors below 10% (dashed line) were considered acceptable.

*Correction of RARE MR images without flipback* (Figure 8): All correction methods reduced the errors to less than 10% for both quantification and contrast, contrary to uncorrected images that showed substantial errors (41-45%) and variabilities (37-42%). None of the calculated mean errors reached a value >8.3% after correction.

The *sensitivity correction* performed best when calculating water content proportions at low $T_1$ values (5.0 ± 2.9%), followed closely by the *hybrid* (6.0 ± 2.7%) and *model-based* (6.6 ± 4.5%) *methods*. All three methods behaved similarly for higher $T_1$ values, with mean errors of approximately 8% (*sensitivity* 8.1 ± 2.9%, *model-based* 8.3 ± 5.9%, *hybrid* 8.1 ± 3.3%). All correction methods improved quantification significantly (*P* value < .0001) when compared to the original data.

When measuring $T_1$ contrast, the *hybrid method* performed best for both water content phantoms (2.4 ± 1.7% high, 4.7 ± 3.8% low). The *sensitivity correction* method performed better than the *model-based method* for the high water content phantom (3.5 ± 2.5% vs. 6.2 ± 5.5%). However, for the low water content comparison,

the *model-based correction* method performed better than the *sensitivity correction* (5.2 ± 3.9% vs. 6.1 ± 3.1%). Similarly, the three described correction methods significantly improved $T_1$ contrast, when compared to the original data (*P* value < .0001).

*Correction of RARE MR images with flipback* (Figure 9): In general, all correction methods performed worse when flipback was enabled in RARE measurements, compared to RARE without flipback. The errors without correction were comparable to the case without the flipback option (40-58%). Their variabilities, however, were spread along a wider range (40-62%).

For quantification, the correction methods performed worse at low $T_1$ relaxation times (overall about 10%: *sensitivity* 11.0 ± 7.6%, *model-based* 10.7 ± 7.9%, *hybrid* 12.2 ± 8.6%) than at higher ones (*sensitivity* 4.8 ± 4.0%, *model-based* 11.4 ± 10.1%, *hybrid* 7.2 ± 6.0%). All correction methods significantly improved quantification when compared to the original data (*P* < .0001).

$T_1$ contrast accuracy was considerably reduced when using flipback during the measurements, with errors approaching 20-30% for high water content. The *sensitivity correction*
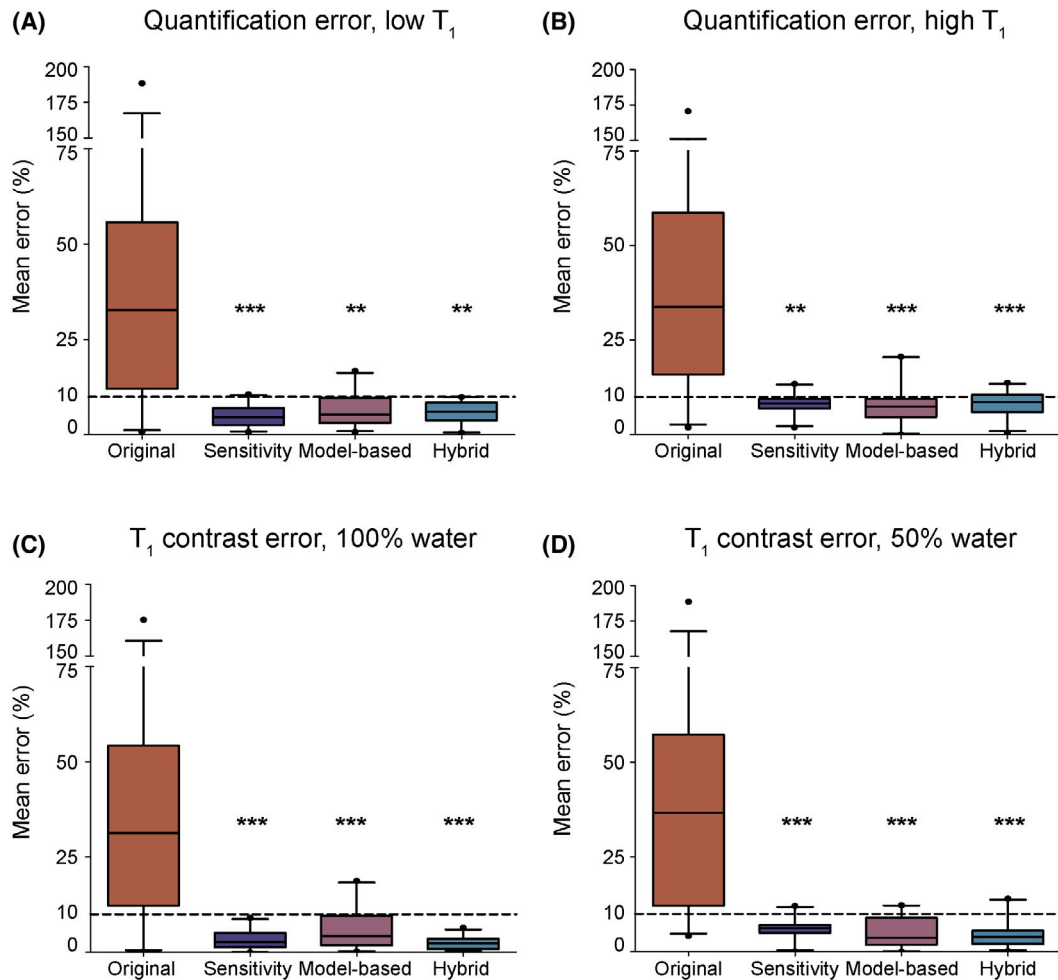
## RARE without flipback



**FIGURE 8** Assessment of quantification and contrast accuracy for Rapid Acquisition with Relaxation Enhancement (RARE) without flipback. Box plot of relative quantification and contrast errors for the original uncorrected images and those corrected with each of the three $B_1$ correction methods. All $B_1$ correction methods reduced the median error from well above 25% to below 10% (dashed line). Whiskers represent the 5 and 95 percentiles. Asterisks indicate statistically significant differences compared to the uncorrected images

method (19.5 ± 9.7%) performed marginally better than the *model-based* (28.9 ± 19.4%) and *hybrid* (28.4 ± 14.5%) *methods*. For higher water content the errors were smaller (8-15%). Similarly, the *sensitivity correction* method (8.3 ± 5.0%) performed slightly better than the other two (*model-based* 15.2 ± 13.2%, *hybrid* 15.2 ± 8.7%). Only the *sensitivity method* significantly improved $T_1$ contrast (*P* value = .0002 and .0003 for high and low proton density, respectively).

## 4 | DISCUSSION

Several methods have been described in the literature to correct $B_1$ inhomogeneities. These methods are especially crucial for images acquired with transceive surface RF coils. The current study extends this work by demonstrating the feasibility

and efficacy of $B_1$ field inhomogeneity correction methods for RARE MRI, for which an analytical SI equation is not available. Our phantom results showed a substantial improvement in image homogeneity after $B_1$ correction using the methods we investigated. We also establish the feasibility of these approaches for samples with more complex structures (ex vivo and in vivo mouse) and in time-constrained scenarios (in vivo). These results demonstrate that images derived from the correction procedures are suitable for accurate $T_1$ contrast and SI quantification purposes, thus opening the way for parametric $T_1$ mapping and X-nuclei quantification using surface transceiver RF coils/probes. Compared to previously developed correction methods,[50-54] the approaches presented and evaluated here are applicable to MR imaging techniques for which no analytical SI equation exists, including but not limited to echo-planar imaging and ultrashort echo time imaging techniques.
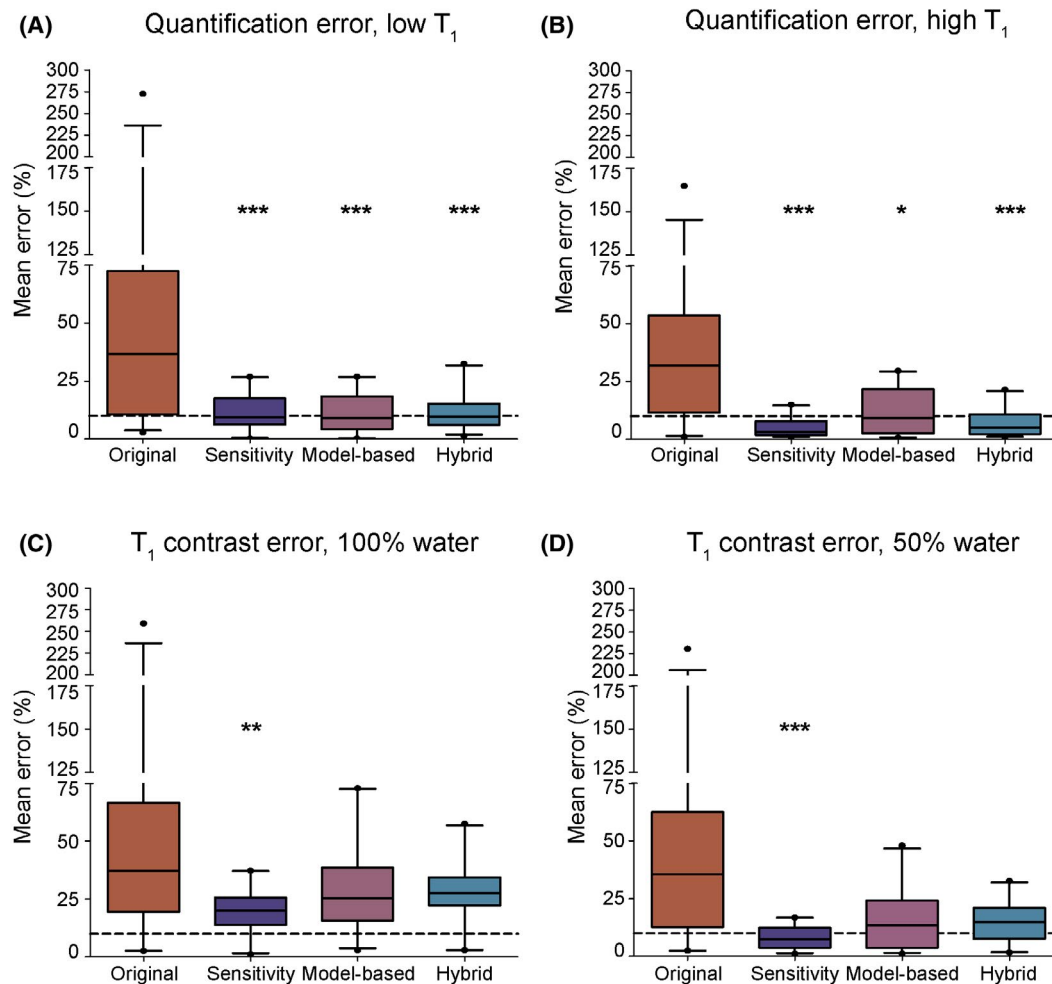
## RARE with flipback



**FIGURE 9** Assessment of quantification and contrast accuracy for Rapid Acquisition with Relaxation Enhancement (RARE) with active flipback. Box plot of relative quantification and contrast errors for the original uncorrected images and those corrected with each of the three $B_1$ correction methods. $B_1$ correction reduced the median quantification error from well above 25% to below 10% (dashed line) but achieved only a modest improvement in the $T_1$ contrast error. Whiskers represent the 5 and 95 percentiles. Asterisks indicate statistically significant differences compared to the uncorrected images

The *sensitivity correction* method is well established in the literature[27] for correction of sensitivity-related inhomogeneities. A typical application is the correction of $B_1^-$ inhomogeneities in a RF coil setup where a volume resonator is used for transmission and a surface RF coil (with or without cryo-cooled technology) for MR signal detection. We demonstrate here that this method is also effective for correction of $B_1^+$ inhomogeneities. The sensitivity correction method includes an inherently linear $B_1^+$ correction, because all images are the product of the transmission and reception capabilities of an RF coil. This concept is supported by the quasi-linear trends shown in our SI model for SI vs. $T_1$ relaxation time, and the linear trends present for the majority of the SI vs. FA range (e.g. between 30°-70° and between 90°-140°).

The two novel $B_1$ correction methods (*model-based*, *hybrid*) we propose use an empirical SI model of the RF pulse sequence. The correction workflow involves using the calculated SI model to adjust the SI to that of the nominal FA, based on the actual FA and $T_1$. This rectifies the inhomogeneities related to RF transmission ($B_1^+$), whereas those related to the RF coil sensitivity ($B_1^-$) are addressed in a separate step using a previously calculated $B_1^-$ map (*model-based*) or using a $B_1^+$-corrected uniform phantom (*hybrid*).

Homogeneity was first assessed calculating the PIU and central SI profiles in the corrected and reference images. These tests revealed a high homogeneity, maintained when comparing the ex vivo phantom to the in vivo situation (difference in mean below 5%). A clear difference was found in the profile comparison (RMSE = 0.12 vs 0.26, ex vivo and in vivo respectively), which might be related to a change in animal position when transferring the animal from [1]H-CRP to reference RF coil. These differences might be also caused

by motion (eg, due to misalignment of the FA map, worse $B_0$ shimming, etc.). Although the option motion averaging was used, it might not have been enough to compensate for bulk motion. Because we were using a RARE-based imaging sequence where the blood signal in large vessels is inherently suppressed due to the use of a spin-echo train, we do not believe the changes in performance to be related to blood flow.[84]

Assessing the accuracy of SI quantification and $T_1$ contrast measurements yielded different results for RARE with and without flipback that drives the equilibrium regimen. Without the driven equilibrium regimen all correction methods reduced the errors to less than 10% for both quantification and $T_1$ contrast, and produced statistically significant improvements compared to the original data. For the driven equilibrium regimen, the errors in the original data were more pronounced, which translated into higher SI quantification and $T_1$ contrast errors after correction. For all three $B_1$ correction methods, errors were around 10% for quantification, but the accuracy of $T_1$ contrast was considerably reduced, with errors up to 20-30% (for high water content). Only the *sensitivity method* improved $T_1$ contrast significantly.

When flipback was inactive, all three methods performed similarly for SI quantification purposes, and yielded improved performance for the low $T_1$ mode. This can be attributed to the reduced $T_1$-weighting at the repetition times used, so that less correction was needed. The *sensitivity correction* method performed slightly better than the other two for SI quantification purposes. The simplicity of this approach makes it preferable for absolute SI quantification. Conversely, our results showed that the *hybrid correction* provides more accuracy when $T_1$ contrast is essential (eg, for contrast-enhanced imaging in inflammatory disease).

Overall, the *hybrid method* performed better than the *model-based* one. Because the only difference between them is the sensitivity profile calculation, we conclude that the simple *sensitivity correction* performs better than the low FA approximation when computing a $B_1^-$ map from measurements. The minor artifacts produced at regions distal to the coil are caused by inaccuracies in the FA information associated with low SNR.

The described *model-based approach* is fundamentally limited by SNR constraints at larger distances from the RF coil, and by the accuracy of the $B_1$ and $T_1$ maps and the polynomial fit. Determining the distance until which a meaningful correction can be achieved is challenging, since it depends on the conditions and scanning parameters used (eg, coil dimensions, SNR, acquisition time). Hence, this distance should be determined by each user, for each specific setup: (1) calculate the central profile plots for each correction and (2) determine at what distance from the coil the corrected profile still follows that of the reference volume RF coil. This will not require extra time, because $T_1$ mapping with the reference RF coil is anyway required for the $B_1$ correction.

Accurate knowledge of $T_1$ and FA is crucial for the precise correction of the $B_1$ inhomogeneities using the *model-based* and *hybrid methods*. For our workflow, we selected readily-available MR imaging protocols (eg, double angle mapping, RARE with variable TR). Limitations are related to the inherent instability associated with the FA and $T_1$ mapping techniques, the lack of an established gold standard, and substantial variability among the different methods. FA mapping depends on the slice excitation profile, $B_0$ homogeneity and other factors,[61] which produce additional uncertainties. Moreover, FA mapping techniques are usually imprecise for low FAs,[85] increasing the FA error at large distances from the RF coil.

$T_1$ mapping is equally challenging and subject to many sources of error. Fundamentally dependent on the FA, it is usually performed using volume resonators or a combination of RF coils for transmit-receive (volume for transmit, surface for receive) to attenuate the effects of $B_1^+$ inhomogeneity. A caveat of these methods (*model-based* and *hybrid*) is the need to acquire a $T_1$ map with each image (in order to consider the $T_1$ contrast of tissues) when removing the field inhomogeneities in $^1$H images. Although $T_1$ mapping is feasible using a cryocooled RF probe,[86] we invested the extra time and used a volume resonator to reduce $T_1$ map errors.

An alternative to calculate the signal evolution (SI model) would be to use extended phase graph[87] or Bloch[88] simulations. Equally, magnetic resonance fingerprinting[89] could be used not only to create the model but also to acquire a $T_1$ and $B_1$ map altogether by changing FA and TR, reducing the amount of scan time needed and producing a tailored correction ("real" $B_1$ map of the phantom/mouse). To our knowledge there are no magnetic resonance fingerprinting-RARE techniques available to date and the development of such MR sequences was out of the scope of this study.

When considering SNR, it is important to bear in mind that these correction methods entail multiplication by a position-dependent matrix of correction factors. Thus, both the signal and the noise will be increased; furthermore, this effect will be different for each image pixel. Therefore, SNR calculations must be performed on the original uncorrected images.

The $B_1$ correction methods presented here have widespread implications. We demonstrated that these methods are not only useful for the specific case of cryogenically cooled RF probes, frequently used to boost SNR in preclinical MRI,[24,40,90] but are also generally applicable for transceive surface RF coils like single-loop RF coils. We demonstrated the applicability of the correction methods in conventional $^1$H brain imaging; however, these methods can also be applied to moving organs, for example, cardiovascular research, as long as the calculated reference power is correct and the maps and images are acquired using a trigger and spatially aligned. These approaches are also highly relevant for quantitative MR of X-nuclei, where absolute SI is important._ENREF_[39,40] For the low-SNR scenarios that are

prevalent in X-nuclei imaging, the procedures that are used to validate the correction methods described in this manuscript (eg, PIU, central profile plots) might not be entirely valid. In these cases, we suggest performing error propagation simulations associated with inaccuracies due to the low SNR or to simply use the sensitivity correction method.

Interestingly, all correction methods we studied here greatly improved SI quantification and image contrast, with only minor differences in performance of the three approaches. The best results were obtained with the *hybrid correction*, but contrary to expectations, even the straightforward *sensitivity correction* performed well. Therefore, one could recommend this last method due to its simplicity. These $B_1$ correction methods permit quantitative SI and $T_1$ contrast measurements with transceiver surface RF coils, using MRI techniques for which analytical SI equations do not exist. This circumvents a key limitation and offers a new approach for correcting $B_1$ inhomogeneity that may be applied for a broad range of biomedical research applications.

## CONFLICT OF INTEREST
Andre Kuehne is an employee of MRI.TOOLS GmbH, Berlin, Germany. Thoralf Niendorf is founder and chief executive officer of MRI.TOOLS GmbH, Berlin, Germany. All other authors declare no conflict of interest.

## DATA AVAILABILITY STATEMENT
The code and data that support the findings of this study are openly available in GitHub at https://github.com/pramosdelgado/B1correction-toolkit.

## ORCID
*Paula Ramos Delgado* https://orcid.org/0000-0003-2009-3024
*João S. Periquito* https://orcid.org/0000-0003-3702-9264
*Sonia Waiczies* https://orcid.org/0000-0002-9916-9572

## REFERENCES
1. Constable R, Henkelman R. Contrast, resolution, and detectability in MR imaging. *J Comput Assist Tomogr*. 1991;15:297-303.
2. Fuderer M. The information content of MR images. *IEEE Trans Med Imaging*. 1988;7:368-380.
3. Redpath T. Signal-to-noise ratio in MRI. *Br J Radiol*. 1998; 71:704-707.
4. Portnoy S, Kale S, Feintuch A, Tardif C, Pike G, Henkelman R. Information content of SNR/resolution trade-offs in three-dimensional magnetic resonance imaging. *Med Phys*. 2009;36:1442-1451.
5. Kale S, Chen X, Henkelman R. Trading off SNR and resolution in MR images. *NMR Biomed*. 2009;22:488-494.
6. Griswold MA, Jakob PM, Heidemann RM, et al. Generalized auto-calibrating partially parallel acquisitions (GRAPPA). *Magn Reson Med*. 2002;47:1202-1210.
7. Pruessmann K, Weiger M, Scheidegger M, Boesiger P. SENSE: Sensitivity encoding for fast MRI. *Magn Reson Med*. 1999;42:952-962.
8. Lustig M, Donoho D, Pauly J. Sparse MRI: The application of compressed sensing for rapid MR imaging. *Magn Reson Med*. 2007;58:1182-1195.
9. Niendorf T, Barth M, Kober F, Trattnig S. From ultrahigh to extreme field magnetic resonance: Where physics, biology and medicine meet. *Magn Reson Mater Phys, Biol Med*. 2016;29:309-311.
10. Ladd M. The quest for higher sensitivity in MRI through higher magnetic fields. *Zeitschrift für medizinische Physik*. 2018;28:1-3.
11. Moser E, Laistler E, Schmitt F, Kontaxis G. Ultra-high field NMR and MRI—The role of magnet technology to Increase sensitivity and specificity. *Front Phys*. 2017;5:33. https://doi.org/10.3389/fphy.2017.0003333.
12. Axel L, Hayes C. Surface coil magnetic resonance imaging. *Archives Internationales de Physiologie et de Biochimie*. 1985;93:11-18.
13. Crowley M, Evelhoch J, Ackermann J. The surface-coil NMR receiver in the presence of homogeneous $B_1$ excitation. *J Magn Reson*. 1985;64:20-31.
14. Hosseinnezhadian S, Frass-Kriegl R, Goluch-Roat S, et al. A flexible 12-channel transceiver array of transmission line resonators for 7 T MRI. *J Magn Reson*. 2018;296:47-59.
15. Pinkerton R, Barberi E, Menon R. Transceive surface coil array for magnetic resonance imaging of the human brain at 4 T. *Magn Reson Med*. 2005;54:499-503.
16. Pinkerton R, Near J, Barberi E, Menon R, Bartha R. Transceive surface coil array for MRI of the human prostate at 4T. *Magn Reson Med*. 2007;57:455-458.
17. Graessl A, Renz W, Hezel F, et al. Modular 32-channel transceiver coil array for cardiac MRI at 7.0T. *Magn Reson Med*. 2014;72:276-290.
18. Rietsch SHG, Pfaffenrot V, Bitz AK, et al. An 8-channel transceiver 7-channel receive RF coil setup for high SNR ultrahigh-field MRI of the shoulder at 7T. *Med Phys*. 2017;44:6195-6208.
19. He X, Ertürk MA, Grant A, et al. First in-vivo human imaging at 10.5T: Imaging the body at 447 MHz. *Magn Reson Med*. 2020;84:289-303. https://doi.org/10.1002/mrm.28131.
20. Ertürk M, Raaijmakers A, Adriany G, Ugurbil K, Metzger G. A 16-channel combined loop-dipole transceiver array for 7 Tesla body MRI. *Magn Reson Med*. 2017;77:884-894.

21. Weinberger O, Winter L, Dieringer MA, et al. Local multi-channel RF surface coil versus body RF coil transmission for cardiac magnetic resonance at 3 Tesla: Which configuration is winning the game? *PLoS ONE*. 2016;11:e0161863.

22. Niendorf T, Paul K, Oezerdem C, et al. W(h)ither human cardiac and body magnetic resonance at ultrahigh fields? Technical advances, practical considerations, applications, and clinical opportunities. *NMR Biomed*. 2016;29:1173-1197.

23. Kovacs H, Moskau D, Spraul M. Cryogenically cooled probes—A leap in NMR technology. *Prog Nucl Magn Reson Spectrosc*. 2005;46:131-155.

24. Baltes C, Radzwill N, Bosshard S, Marek D, Rudin M. Micro MRI of the mouse brain using a novel 400MHz cryogenic quadrature RF probe. *NMR Biomed*. 2009;22:834-842.

25. Niendorf T, Pohlmann A, Reimann HM, et al. Advancing cardiovascular, neurovascular, and renal magnetic resonance imaging in small rodents using cryogenic radiofrequency coil technology. *Front Pharmacol*. 2015;12:255.

26. Carvalho V, Hertanu A, Grélard A, et al. MRI assessment of multiple dipolar relaxation time ($T_{1D}$) components in biological tissues interpreted with a generalized inhomogeneous magnetization transfer (ihMT) model. *J Magn Reson*. 2020;311:106668.

27. Axel L, Constantini J, Listerud J. Intensity correction in surface-coil MR imaging. *Am J Roentgenol*. 1987;148:418-420.

28. Wicks D, Barker G, Tofts P. Correction of intensity nonuniformity in MR images of any orientation. *Magn Reson Imaging*. 1993;11:183-196.

29. McVeigh E, Bronskill M, Henkelman R. Phase and sensitivity of receiver coils in magnetic resonance imaging. *Med Phys*. 1986;13:806-814.

30. Tincher M, Meyer C, Gupta R, Williams D. Polynomial modeling and reduction of RF body coil spatial inhomogeneity in MRI. *IEEE Trans Med Imaging*. 1993;12:361-365.

31. Meyer CR, Bland PH, Pipe J. Retrospective correction of intensity inhomogeneities in MRI. *IEEE Trans Med Imaging*. 1995;14:36-41.

32. Haselgrove J, Prammer M. An algorithm for compensation of surface-coil images for sensitivity of the surface coil. *Magn Reson Imaging*. 1986;4:469-472.

33. Moyher S, Vigneron D, Nelson S. Surface coil MR imaging of the human brain with an analytic reception profile correction. *J Magn Reson Imaging*. 1995;5:139-144.

34. Narayana P, Brey W, Kulkarny M, Sievenpiper C. Compensation for surface coil sensitivity variation in magnetic resonance imaging. *Magn Reson Imaging*. 1988;6:271-274.

35. Vaidya M, Collins C, Sodickson D, Brown R, Wiggins G, Lattanzi R. Dependence of $B_1^+$ and $B_1^-$ field patterns of surface coils on the electrical properties of the sample and the MR operating frequency. *Concept Magn Reson B*. 2016;46B:25-40.

36. Keltner J, Carlson J, Roos M, Wong S, Wong T, Budinger T. Electromagnetic fields of surface coil *in vivo* NMR at high frequencies. *Magn Reson Med*. 1991;22:467-480.

37. Boulant N. $T_1$ and $T_2$ effects during radio-frequency pulses in spoiled gradient echo sequences. *J Magn Reson*. 2009;197:213-218.

38. Dieringer MA, Deimling M, Santoro D, et al. Rapid parametric mapping of the longitudinal relaxation time $T_1$ using two-dimensional variable flip angle magnetic resonance imaging at 1.5 Tesla, 3 Tesla, and 7 Tesla. *PLoS ONE*. 2014;9:e91318.

39. Lommen J, Konstandin S, Krämer P, Schad L. Enhancing the quantification of tissue sodium content by MRI: Time-efficient

40. Waiczies S, Millward JM, Starke L, et al. Enhanced fluorine-19 MRI sensitivity using a cryogenic radiofrequency probe: Technical developments and *ex vivo* demonstration in a mouse model of neuroinflammation. *Sci Rep*. 2017;7:9808.

41. de Graaf R, Nicolay K. Adiabatic rf pulses: Applications to *in vivo* NMR. *Magn Reson Med*. 1998;40:690-696.

42. Baldanchani P, Pauly J, Spielman D. Designing adiabatic radio frequency pulses using the Shinnar–Le Roux algorithm. *Magn Reson Med*. 2010;64:843-851.

43. Zivkovic I, Teeuwisse W, Slobozhanyuk A, Nenasheva E, Webb A. High permittivity ceramics improve the transmit field and receive efficiency of a commercial extremity coil at 1.5 Tesla. *J Magn Reson*. 2019;299:59-65.

44. Brink W, van der Jagt A, Versluis M, Verbist B, Webb A. High permittivity dielectric pads improve high spatial resolution magnetic resonance imaging of the inner ear at 7 T. *Invest Radiol*. 2014;49:271-277.

45. O'Brien K, Magill A, Delacoste J, et al. Dielectric pads and low-$B_1^+$ adiabatic pulses: Complementary techniques to optimize structural $T_1$w whole-brain MP2RAGE scans at 7 Tesla. *J Magn Reson Imaging*. 2014;40:804-812.

46. O'Reilly T, Webb A, Brink W. Practical improvements in the design of high permittivity pads for dielectric shimming in neuroimaging at 7 T. *J Magn Reson*. 2016;270:108-114.

47. van der Bergen B, van der Berg C, Bartels L, Lagendijk J. 7 T body MRI: $B_1$ shimming with simultaneous SAR reduction. *Phys Med Biol*. 2007;52:5429-5441.

48. Winkler S, Rutt B. Practical methods for improving $B_1^+$ homogeneity in 3 Tesla breast imaging. *J Magn Reson Imaging*. 2015;41:992-999.

49. Yang QX, Mao W, Wang J, et al. Manipulation of image intensity distribution at 7.0 T: Passive RF shimming and focusing with dielectric materials. *J Magn Reson Imaging*. 2006;24:197-202.

50. Vernikouskaya I, Pochert A, Lindén M, Rasche V. Quantitative $^{19}$F MRI of perfluoro-15-crown-5-ether using uniformity correction of the spin excitation and signal reception. *Magn Reson Mater Phys, Biol Med*. 2019;32:25-36.

51. van Schie J, Lavini C, van Vliet L, Vos F. Feasibility of a fast method for $B_1$-inhomogeneity correction for FSPGR sequences. *Magn Reson Imaging*. 2015;33:312-318.

52. Wang J, Qiu M, Constable R. *In vivo* method for correcting transmit/receive nonuniformities with phased array coils. *Magn Reson Med*. 2005;53:666-674.

53. Collewet G, Davenel A, Toussaint C, Akoka S. Correction of intensity nonuniformity in spin-echo $T_1$-weighted images. *Magn Reson Imaging*. 2002;20:365-373.

54. Cooper M, Nguyen T, Spincemaille P, Prince M, Weinsaft J, Wang Y. Flip angle profile correction for $T_1$ and $T_2$ quantification with look-locker inversion recovery 2D SSFP imaging. *Magn Reson Med*. 2012;68:1579-1585.

55. Ma D, Coppo S, Chen Y, et al. Slice profile and $B_1$ corrections in 2D magnetic resonance fingerprinting. *Magn Reson Med*. 2017;78:1781-1789.

56. Deoni S. Correction of main and transmit magnetic field (B0 and B1) inhomogeneity effects in multicomponent-driven equilibrium single-pulse observation of T1 and T2. *Magn Reson Med*. 2011;65:1021-1035.

57. Insko E, Bolinger L. Mapping of the radiofrequency field. *J Magn Reson*. 1993;103A:82-85.

58. Akoka S, Franconi F, Seguin F, Le Pape A. Radiofrequency map of an NMR coil by imaging. *Magn Reson Imaging*. 1993;11:437-441.

59. Morrell G. A phase-sensitive method of flip angle mapping. *Magn Reson Med*. 2008;60:889-894.

60. Yarnykh V. Actual flip-angle imaging in the pulsed steady state: A method for rapid three-dimensional mapping of the transmitted radiofrequency field. *Magn Reson Med*. 2007;57:192-200.

61. Wang J, Mao W, Qiu M, Smith M, Constable R. Factors influencing flip angle mapping in MRI: RF pulse shape, slice-select gradients, off-resonance excitation, and $B_0$ inhomogeneities. *Magn Reson Med*. 2006;56:463-468.

62. Stollberger R, Wach P. Imaging of the active B1 field in vivo. *Magn Reson Med*. 1996;35:246-251.

63. Cunningham C, Pauly J, Nayak K. Saturated double-angle method for rapid $B_1^+$ mapping. *Magn Reson Med*. 2006;55:1326-1333.

64. Wang D, Heberlein K, LaConte S, Hu X. Inherent insensitivity to RF inhomogeneity in FLASH imaging. *Magn Reson Med*. 2004;52:927-931.

65. Bernstein M. Gradient echo. In: Bernstein M, King K, Zhou X, eds. *Handbook of MRI Pulse Sequences*. Burlington, MA, San Diego, CA and London: Elsevier Academic Press; 2004:579-605.

66. Hennig J, Nauerth A, Friedburg H. RARE imaging: A fast imaging method for clinical MR. *Magn Reson Med*. 1986;3:823-833.

67. Conturo T, Beth A, Arenstorf R, Price R. Simplified mathematical description of longitudinal recovery in multiple-echo sequences. *Magn Reson Med*. 1987;4:282-288.

68. Meara S, Barker G. Evolution of the longitudinal magnetization for pulse sequences using a fast spin-echo readout: Application to fluid-attenuated inversion-recovery and double inversion-recovery sequences. *Magn Reson Med*. 2005;54:241-245.

69. Breuer F, Blaimer M, Heidemann R, Mueller M, Griswold M, Jakob P. Controlled aliasing in parallel imaging results in higher acceleration (CAIPIRINHA) for multi-slice imaging. *Magn Reson Med*. 2005;53:684-691.

70. Skare S, Holdsworth S, Lilja A, Bammer R. Image domain propeller fast spin echo. *Magn Reson Imaging*. 2013;31:385-395.

71. Zhou X, Liang Z, Gewalt S, Cofer G, Lauterbur P, Johnson G. A fast spin echo technique with circular sampling. *Magn Reson Med*. 1998;39:23-27.

72. Altbach MI, Outwater EK, Trouard TP, et al. Radial fast spin-echo method for $T_2$-weighted imaging and $T_2$ mapping of the liver. *J Magn Reson Imaging*. 2002;16:179-189.

73. Busse RF, Brau ACS, Vu A, et al. Effects of refocusing flip angle modulation and view ordering in 3D fast spin echo. *Magn Reson Med*. 2008;60:640-649.

74. Reeder SB, Pineda AR, Wen Z, et al. Iterative decomposition of water and fat with echo asymmetry and least-squares estimation (IDEAL): Application with fast spin-echo imaging. *Magn Reson Med*. 2005;54:636-644.

75. Oshio K, Feinberg D. GRASE (Gradient- and Spin Echo) imaging: A novel fast MRI technique. *Magn Reson Med*. 1991;20:344-349.

76. Robson D, Gatehouse P, Bydder M, Bydder G. Magnetic resonance: An introduction to ultrashort TE (UTE) imaging. *J Comput Assist Tomogr*. 2003;27:825-846.

77. Mansfield P. Multi-planar image formation using NMR spin echoes. *J Phys C: Solid State Phys*. 1977;10:55-58.

78. Waiczies H, Lepore S, Drechsler S, et al. Visualizing brain inflammation with a shingled-leg radio-frequency head probe for $^{19}F/^1H$ MRI. *Sci Rep*. 2013;3:1280.

79. *Polyfitn* [computer program]. Version 1.3. File Exchange. Natick, MA: The MathWorks, Inc. 2016.

80. Ibrahim T, Hue Y, Tang L. Understanding and manipulating the RF fields at high field MRI. *NMR Biomed*. 2009;22:927-936.

81. Pauly J, Nishimura D, Macovski A. A k-space analysis of small-tip-angle excitation. *J Magn Reson*. 1989;81:43-56.

82. Manjón J, Coupé P, Martí-Bonmatí L, Collins D, Robles M. Adaptive non-local means denoising of MR images with spatially varying noise levels. *J Magn Reson Imaging*. 2010;31:192-203.

83. Price R, Axel L, Morgan T, et al. Quality assurance methods and phantoms for magnetic resonance imaging: Report of AAPM nuclear magnetic resonance task group No. 1. *Med Phys*. 1990;17:287-295.

84. Feinberg DA, Mills CM, Posin JP, et al. Multiple spin-echo magnetic resonance imaging. *Radiology*. 1985;155:437-442.

85. Balezeau F, Eliat P, Cayamo A, Saint-Jalmes H. Mapping of low flip angles in magnetic resonance. *Phys Med Biol*. 2011;56:6635-6647.

86. Khalil AA, Mueller S, Foddis M, et al. Longitudinal $^{19}F$ magnetic resonance imaging of brain oxygenation in a mouse model of vascular cognitive impairment using a cryogenic radiofrequency coil. *Magn Reson Mater Phys, Biol Med*. 2019;32:105-114.

87. Weigel M. Extended phase graphs: Dephasing, RF pulses, and echoes—Pure and simple. *J Magn Reson Imaging*. 2015;41:266-295.

88. Bloch F. Nuclear induction. *Phys Rev*. 1946;70:460-474.

89. Ma D, Gulani V, Seiberlich N, et al. Magnetic resonance fingerprinting. *Nature*. 2013;495:187-192.

90. Ratering D, Baltes C, Nordmeyer-Massner J, Marek D, Rudin M. Performance of a 200-MHz cryogenic RF probe designed for MRI and MRS of the murine brain. *Magn Reson Med*. 2008;59:1440-1447.